

# Giant Strain Response of Charge Modulation and Singularity in a Kagome Superconductor

Chun Lin,<sup>1,\*</sup> Armando Consiglio,<sup>2</sup> Ola Kenji Forslund,<sup>1,3</sup> Julia Küspert,<sup>1</sup> M. Michael Denner,<sup>1</sup> Hechang Lei,<sup>4</sup> Alex Louat,<sup>5</sup> Matthew D. Watson,<sup>5</sup> Timur K. Kim,<sup>5</sup> Cephise Cacho,<sup>5</sup> Dina Carbone,<sup>6</sup> Mats Leandersson,<sup>6</sup> Craig Polley,<sup>6</sup> Thiagarajan Balasubramanian,<sup>6</sup> Domenico Di Sante,<sup>7,8</sup> Ronny Thomale,<sup>2</sup> Zurab Guguchia,<sup>9</sup> Giorgio Sangiovanni,<sup>2</sup> Titus Neupert,<sup>1</sup> and Johan Chang<sup>1</sup>

<sup>1</sup>*Physik-Institut, Universität Zürich, Winterthurerstrasse 190, CH-8057 Zürich, Switzerland*

<sup>2</sup>*Institut für Theoretische Physik und Astrophysik and Würzburg-Dresden Cluster of Excellence ct.qmat, Universität Würzburg, 97074 Würzburg, Germany*

<sup>3</sup>*Department of Physics and Astronomy, Uppsala University, Box 516, SE-75120 Uppsala, Sweden*

<sup>4</sup>*Department of Physics and Beijing Key Laboratory of Opto-electronic Functional Materials & Micro-nano Devices, Renmin University of China, Beijing 100872, China*

<sup>5</sup>*Diamond Light Source Ltd, Harwell Science and Innovation Campus, Didcot, OX110FB, United Kingdom*

<sup>6</sup>*MAX IV Laboratory, Lund University, 22100 Lund, Sweden*

<sup>7</sup>*Department of Physics and Astronomy, University of Bologna, 40127 Bologna, Italy*

<sup>8</sup>*Center for Computational Quantum Physics, Flatiron Institute, 162 5th Avenue, New York, NY 10010, USA*

<sup>9</sup>*Laboratory for Muon Spin Spectroscopy, Paul Scherrer Institute, CH-5232 Villigen PSI, Switzerland*

**Tunable quantum materials hold great potential for applications. Of special interest are materials in which small lattice strain induces giant electronic responses. The kagome compounds  $AV_3Sb_5$  ( $A = K, Rb, Cs$ ) provide a testbed for such singular electronic states. In this study, through angle-resolved photoemission spectroscopy, we provide comprehensive spectroscopic measurements of the giant responses induced by compressive and tensile strains on the charge-density-wave (CDW) order parameter and high-order van Hove singularity (HO-VHS) in  $CsV_3Sb_5$ . We observe a tripling of the CDW gap magnitudes with  $\sim 1\%$  strain, accompanied by the changes of both energy and mass of the saddle-point fermions. Our results reveal an anticorrelation between the unconventional CDW order parameter and the mass of a HO-VHS, and highlight the role of the latter in the superconducting pairing. The giant electronic responses uncover a rich strain tunability of the versatile kagome system in studying quantum interplays under lattice perturbations.**

Uniaxial strain possesses a promising potential for engineering the band structure and hence physical properties of quantum materials [1–5]. Near quantum critical points, even small strain stimulus can induce dramatic electronic responses [3–5]. Yet, spectroscopic demonstrations of such effects remain challenging [5].

Recently discovered kagome superconductors  $AV_3Sb_5$  ( $A = K, Rb, Cs$ ) provide an uncharted ground for studies of symmetry-breaking states emerging from electronic

correlations [6]. Charge density wave (CDW) [7–9] and superconductivity (SC) [10–12] are currently discussed intensely. The unconventional CDW in  $AV_3Sb_5$  is characterized by features such as the chiral responses [13, 14], electronic nematicity [15, 16], and breaking of time-reversal symmetry [12, 17]. Pressure-tunable pairing symmetries [12] and double  $T_c$  domes [10] also point to an unconventional nature of SC.

Despite intensive studies, the CDW origin and SC pairing mechanism in  $AV_3Sb_5$  are still debated. Both instabilities may be linked to the presence of a high-order van Hove singularity (HO-VHS) [18–20]. That is a saddle point with vanishingly small band curvature. A HO-VHS features power-law divergent density of states (DOS) and further enhanced correlation effects [18]. Its manifestation in the charge-ordered  $AV_3Sb_5$  offers a fine quantum tuning knob. Any intimate connections to a HO-VHS would disclose the nature of associated broken-symmetry states. Direct measurements that reveal the interplay of lattice and electronic degrees of freedom are therefore in high demand.

Here, we report angle-resolved photoemission spectroscopy (ARPES) observations of giant CDW responses to strain accompanied by a direct tuning of HO-VHS in  $CsV_3Sb_5$ . Improved ARPES band maps, assisted by density functional theory (DFT), allow a detailed examination of the low-energy electronic structure. Through both uniaxial compressive and tensile strains, we observe a giant response from the CDW order parameter. That is, the energy gap is reduced by a factor of three (from  $\sim 150$  to 55 meV) as the strain is adjusted from compressive to tensile ( $\pm 0.6\%$ ). Simultaneously, the mass of fermions at a HO-VHS is enhanced, whose energy is driven towards  $E_F$ . The HO saddle point splits into two upon a compression. While a nearly ideal HO-VHS is realised with a tensile strain. These observations demonstrate an uncon-

---

\* [chun.lin@physik.uzh.ch](mailto:chun.lin@physik.uzh.ch)

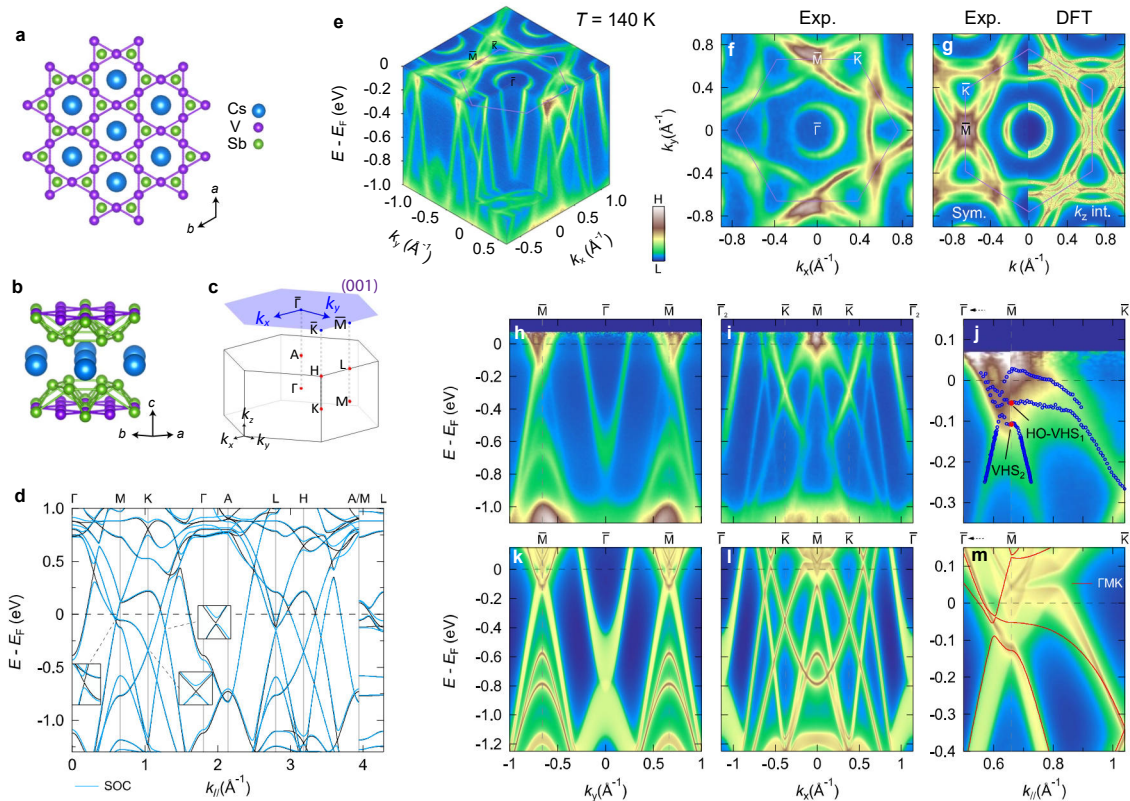
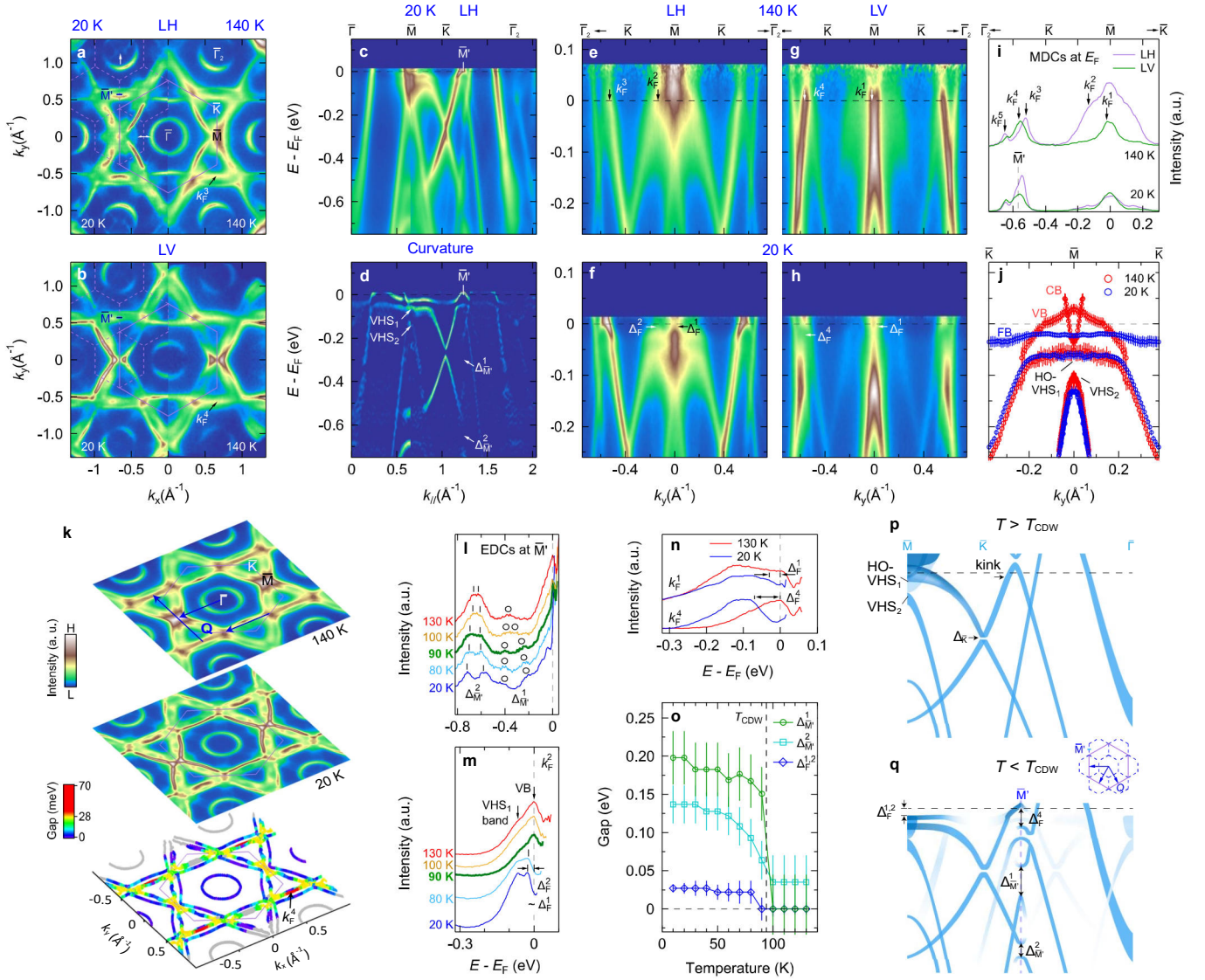


FIG. 1. **Band structure of the kagome superconductor  $\text{CsV}_3\text{Sb}_5$  above  $T_{\text{CDW}}$ .** **a,b**, Top and side views of the quasi two-dimensional (2D) crystal structure. **c**, Three-dimensional (3D) Brillouin zone (BZ) and its 2D projection. **d**, Band structure along high-symmetry paths calculated by density functional theory (DFT) without and with spin-orbit coupling (SOC). **e**, 3D overview of the experimental ARPES band structure. **f**, Experimental (Exp.) Fermi surface (FS). **g**, Comparison between the experimental and the calculated  $k_z$  integrated (int.) FSs. The experimental FS is mirror symmetrized (Sym.) with respect to  $\bar{M}\bar{K}$  and  $\bar{\Gamma}\bar{M}$  which effectively minimizes the matrix-element effects (Supplementary Fig. S2). Purple hexagons in **e-g** indicate the surface BZ. **h,i**, Experimental spectra divided by the Fermi-Dirac function (Supplementary Fig. S3 and Methods) along  $\bar{\Gamma}\bar{M}$  and  $\bar{M}\bar{K}\bar{\Gamma}$ . **j**, Magnified spectrum along  $\bar{\Gamma}\bar{M}\bar{K}$ , where the quasi-particle peaks near  $E_F$  are plotted around the  $\bar{M}$  point showing two van Hove singularities (VHS<sub>1,2</sub>) as indicated by the red points. VHS<sub>1</sub> is of high-order (HO) nature, see details in Supplementary Fig. S4 and Methods. **k-m**, Correspondingly calculated  $k_z$ -integrated dispersions with SOC. Measurement temperature was set at  $T = 140$  K, see Methods for more detailed experimental conditions. The colour bar represents ARPES intensities from high (H) to low (L) in arbitrary units.

ventional strain-sensitive charge modulation with strong electronic anticorrelations coupling to a highly tunable HO-VHS. Given the rising SC  $T_c$  with tensile strain, our results of enhanced electronic correlations at  $E_F$  suggest the important role of a HO singularity in the SC pairing in  $\text{CsV}_3\text{Sb}_5$ .

The quasi two-dimensional (2D) crystal structure of  $\text{CsV}_3\text{Sb}_5$  facilitates ARPES observations on (001) surfaces (Fig. 1a-c). Band structure observed above the CDW temperature ( $T_{\text{CDW}} \sim 94$  K) and first-principle calculations by DFT are presented in Fig. 1d-m. We focus on the spectra near  $k_z = 0$  throughout this study, see Supplementary Fig. S1 for the discussions about  $k_z$  dispersions. The Fermi surface is composed of a Sb  $p$ -dominated electron pocket centering the  $\bar{\Gamma}$  point and V  $d$ -dominated kagome-net bands near the Brillouin zone (BZ) boundaries [21] (Fig. 1d-g). In Fig. 1g, we mirror

symmetrised the Fermi surface to alleviate photoemission matrix-element effect which alternates spectral weights of different bands when crossing BZ boundaries (Supplementary Fig. S2). As such, the observation matches nicely with  $k_z$  integrated DFT (Fig. 1g). Figure 1e,h,i shows high-symmetry band dispersions which agree well with the DFT (Fig. 1k,l). Note that, all dispersions are divided by a resolution-convolved Fermi-Dirac function to recover single-particle spectral functions allowed by thermal populations (Supplementary Fig. S3). In Fig. 1j,m, we detail the two VHSs near  $E_F$ . Band structure around the  $\bar{M}$  point is extracted from spectral peaks (Supplementary Fig. S4). Polynomial fits for the VHS<sub>1</sub> band closer to  $E_F$  validate its high-order nature, consistent with previous reports [19, 20]. The main spectral peaks along  $\bar{M}\bar{K}$  disperse across  $E_F$ , which is identified as a valence band crossing between M and L points in line



**FIG. 2. Temperature-dependent band structure across the CDW transition.** **a,b**, Fermi surfaces acquired at 20 K and 140 K with linear horizontal (LH) and vertical (LV) light polarizations as indicated. Solid and dashed hexagons depict the pristine and CDW-reduced surface BZs with  $\bar{M}'$  indicating the new BZ boundary. White arrows exemplify CDW band foldings between  $\bar{\Gamma}$  and  $\bar{M}$  points. **c,d**, Band dispersion along  $\bar{\Gamma}\bar{M}\bar{K}\bar{\Gamma}$  and its curvature plot (Methods) collected at 20 K with LH polarization. **e-h**, Temperature- and polarization-dependent low-energy  $\bar{M}\bar{K}$  band structures. **i**, Polarization-dependent momentum distribution curves (MDCs) at  $E_F$  along  $\bar{M}\bar{K}\bar{\Gamma}$ . **j**, Temperature-dependent low-energy band structures near VHSs, see details in Supplementary Fig. S4 and Methods. Conduction band (CB), valence band (VB), and flat band (FB) are indicated. **k**, Energy gaps at Fermi surface (Supplementary Fig. S7 and Methods). The Fermi surfaces are polarization-integrated and mirror symmetrised (see also Fig. 1g). The arrows indicate the equivalent nesting wave vectors ( $\mathbf{Q}$ ) in the extended/reduced zone scheme. **l-n**, Temperature dependences of energy distribution curves (EDCs) at momentum positions as indicated in **i**. The vertical bars or circles indicate the peak positions defining the spectral gaps. **o**, Temperature dependence of Energy gaps. CDW transition temperature ( $T_{CDW} \sim 94$  K) is indicated by the vertical dash line. **p,q**, Schematics of temperature evolution of  $\bar{M}\bar{K}\bar{\Gamma}$  band structure deduced from Fig. 1i and **c-h**. Band-folding gaps at  $\bar{M}'$  are labeled as  $\Delta_{\bar{M}'}^i$  ( $i$ : integer). Fermi momenta and corresponding gaps are marked as  $k_F^i$  and  $\Delta_F^i$  respectively. All spectra were divided by the Fermi-Dirac function, see Methods for more detailed experimental conditions. The spectral and gap colour bars represent ARPES intensities from high (H) to low (L) in arbitrary units and magnitude of energy gap at  $E_F$ , respectively.

with the slab calculation in Fig. 1m (see also Fig. 2j). Notably, experiments reveal overall narrower band widths than DFT as indicated by the energy ranges in Fig. 1h-m.

In Fig. 2, we present a temperature evolution of band structure across the CDW transition. Side-by-side comparisons are shown in Fig. 2a,b where the Fermi surfaces were collected above and below  $T_{CDW}$  with different light

polarizations. When entering the CDW state, we observe a Fermi-surface reconstruction manifested as the emergence of “shadow” bands (white arrows in Fig. 2a). These folding bands with rotation-symmetry breaking (Supplementary Fig. S5) are consistent with the recent observation of electronic nematicity driven by the 3D CDW with  $c$ -axis  $\pi$ -phase shift in  $\text{KV}_3\text{Sb}_5$  [22].

Low-temperature dispersions along  $\bar{\Gamma}\bar{M}\bar{K}\bar{\Gamma}$  is plotted in Fig. 2c,d. The  $\bar{M}'$  point indicates the boundary of CDW reconstructed new BZ (dashed hexagons in Fig. 2a,b). The pronounced CDW-folded bands with respect to the  $\bar{M}'$  as well as rich folding gaps suggest a long-range charge modulation (Supplementary Fig. S6). We denote the energy gaps at the  $\bar{M}'$  as  $\Delta_{\bar{M}'}^i$  ( $i$ : integer), whose temperature dependences confirm the CDW origin (Fig. 2l,o). Besides, a significant fluctuation well above  $T_{\text{CDW}}$  is suggested by the possible opening of  $\Delta_{\bar{M}'}^2$  at 130 K. In Fig. 2e-h, we present the CDW effects on the low-energy states near  $E_F$  with Fermi momenta ( $k_F^i$ , Fig. 2i) and corresponding gaps ( $\Delta_F^i$ ) indicated. Below  $T_{\text{CDW}}$ ,  $\Delta_F^i$  opens at  $k_F^i$  where  $i = 1, 2$ , and 4 (Fig. 2m-o). The momentum structure of gaps at  $E_F$  is shown in Fig. 2k. The  $k_F$  and resulting Fermi-surface contour are first extracted at 140 K (Supplementary Fig. S7). Energy gaps at  $k_F$  are therefore deduced along this contour, mostly concentrating near the  $\bar{M}$  point ( $28 \pm 5$  meV) in line with  $\text{KV}_3\text{Sb}_5$  [23]. Additionally, a gap doubling at  $k_F^4$  ( $\Delta_F^4 = 70 \pm 10$  meV) is uniquely identified on the Fermi-surface sheet visible only with a vertical light polarization (Fig. 2b,h,n). Such a large gap on this well nested Fermi-surface sheet is expected for an electronically driven instability, as shown by the nesting wave vectors in Fig. 2k (see also Supplementary Figs. S7,S8).

The gap openings are accompanied by the electronic renormalizations near the VHSs. This is demonstrated by the extracted band structure along  $\bar{M}\bar{K}$  (Fig. 2j and Supplementary Fig. S4j,k). A conduction/valence band (CB/VB) and a flat band (FB) are identified at high and low temperatures, respectively. The FB is attributed from the CDW renormalizations around  $E_F$  manifested as a continuous gapping of the CB and VB (Fig. 2j,m and the notes in Supplementary Fig. S6). Although both VHSs show a tendency of energy lowering in the CDW state (Fig. 2j). The HO-VHS<sub>1</sub> band is abnormally lifted near the  $\bar{K}$  point leading to a narrower bandwidth and flattening when approaching the  $\bar{M}$  point. This together with the FB indicate further enhanced electronic correlations below  $T_{\text{CDW}}$  with a mass acquisition. In Fig. 2p,q, we sketch the CDW effects manifested by the band foldings, gap openings, and renormalized heavy fermions near the VHSs.

Next, we turn to observations obtained with strains applied along the  $a$ -axis. The strain cell, simulations of strain, and strain-calibration curve are shown in Fig. 3a-d (see Methods for the technical information). In Fig. 3e-g, we show the band-structure evolution (Fig. 3e-g) upon

compressive and tensile strain applications. Close-ups along the  $\bar{M}\bar{K}$  path near  $E_F$  are shown in Fig. 3h-j. Superimposed are the band structures extracted from spectral peaks, which are summarized in Fig. 3k and fitted for the VHS<sub>1,2</sub>-derived bands in Fig. 3l (Supplementary Figs. S9,S10). A tensile strain shifts both VHSs towards  $E_F$ —see the peaks of energy distribution curves (EDCs) in Fig. 3m. Strikingly, the HO-VHS<sub>1</sub> band undergoes a curvature change while maintaining other portions nearly intact. That is, it exhibits a flat and hole-like dispersion near the  $\bar{M}$  point upon tensile strain. Whereas a transition to the electron character appears with the compression leading to two new VHSs as indicated by the arrows in Fig. 3l. In Fig. 3n, as a function of strain, we plot the energy positions of VHS<sub>1,2</sub> as well as the second-order polynomial fitting coefficient ( $C_2$ ) for the VHS<sub>1</sub> band.  $C_2$  describes the band curvature in the vicinity of VHS<sub>1</sub> through  $\omega(k)''|_{k=0} = 2C_2$ , where  $\omega(k)$  is the dispersion relationship. A smaller  $C_2$  thus indicates a flatter and higher-order dispersion (Methods or Supplementary Fig. S10). The drastic reduction of  $C_2$  suggests that the high-order character of VHS<sub>1</sub> is rapidly enhanced with tensile strain (Fig. 3n, see reproducibility in Supplementary Fig. S11).

Strain effects on the CDW-related electronic states along  $\bar{M}\bar{K}\bar{\Gamma}$  are shown in Fig. 4a-c. Followed in Fig. 4d-f are strain-dependent EDCs at  $\bar{M}'$ ,  $k_F^1$ , and  $\bar{\Gamma}_2$ . A direct CDW response to strain is observed—both the band-folding gap at  $\bar{M}'$  ( $\Delta_{\bar{M}'}^{1,2}$ ) and Fermi-surface gap at  $k_F^1$  ( $\Delta_F^1$ ) fade away as strain changes from compressive to tensile. Such a CDW suppression is further supported by a simultaneous diminishing of the CDW-folded bands near  $\bar{\Gamma}_2$  (horizontal arrows in Fig. 4f, see reversibility in Supplementary Fig. S11). Additionally, the band bottom at  $\bar{\Gamma}_2$  is lifted by  $\sim 0.1$  eV (dashed arrow in Fig. 4f). In Fig. 4g,h, we summarise the overall band-structure evolution under uniaxial strains, featured by the tuning of VHSs (Fig. 3) and a pronounced CDW response.

To quantify the changes of CDW order parameter, Fig. 5a shows strain evolutions of gap magnitudes—defined as either quasi-particle peak separation ( $\Delta_{\bar{M}'}^2$ ) or spectral-weight suppression ( $\Delta_{\bar{M}'}^1$ , and  $k_F^1$  as represented by the grey shaded areas in Fig. 4d,e, see Methods). Regardless of definitions, the CDW gaps display a giant strain response, i.e., the gap magnitudes change by a factor of three with only  $\sim 1\%$  strain variation.

The upward shifts of VHSs at the  $\bar{M}$  point agree well with the in-plane strain calculations with a constant  $c$ -axis [25]. By contrast, the large energy lifts of Sb- $p$  pocket at the  $\bar{\Gamma}$  point (Fig. 4f,h) are consistent with the hydrostatic-pressure calculations dominated by the fast shrinkage of  $c$  lattice parameter [26]. These results indicate that both in-plane and out-of-plane lattice variations play important roles in pressure tuning the band structure. Furthermore, the distinct energy changes for different bands rule out a simple chemical-

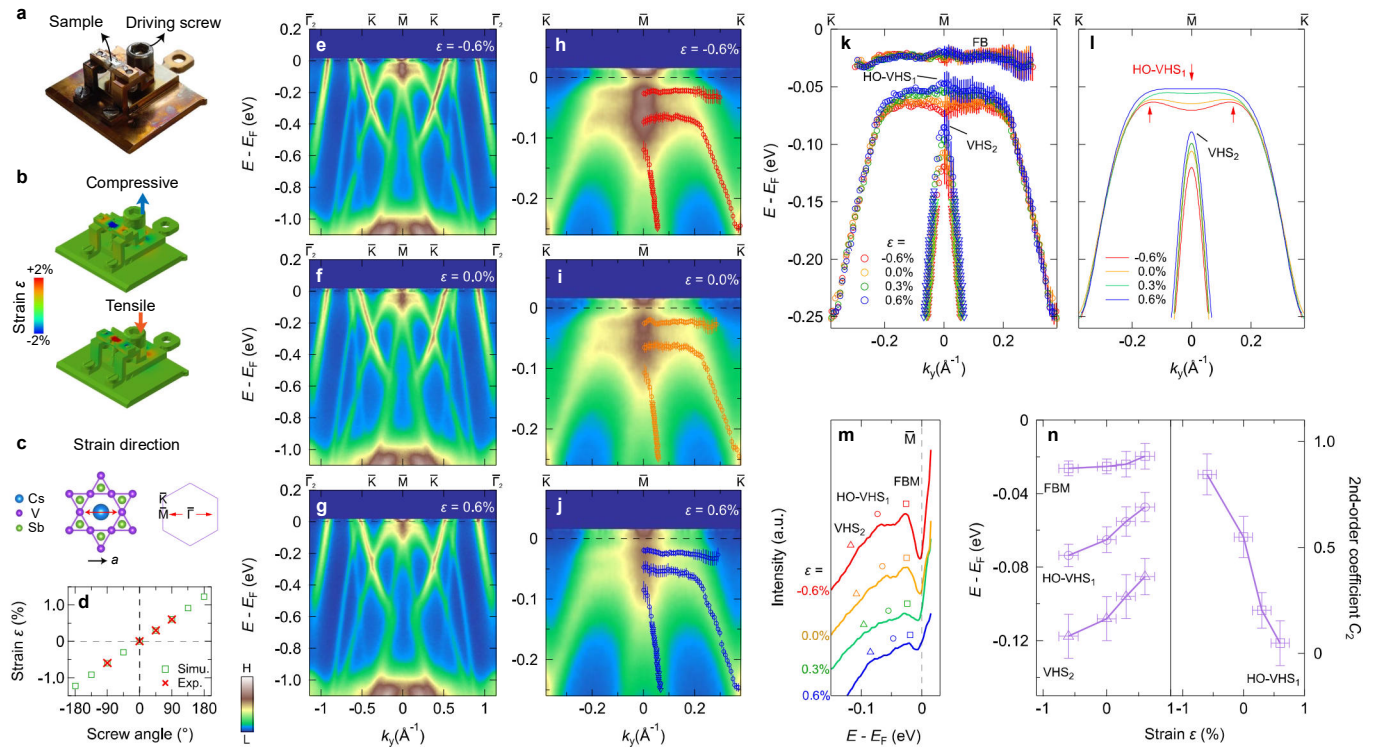


FIG. 3. **Strain tuning of the VHSs.** **a**, *In-situ* strain device designed for compressive and tensile strain ( $\epsilon$ ) applications. **b**, Finite-element simulations for the cases of compressive ( $\epsilon < 0$ ) and tensile ( $\epsilon > 0$ ) strains. **c**, Strain direction in real and reciprocal spaces as indicated by red arrows. **d**, Strain as a function of driving-screw rotation angle estimated from simulation (Simu.). Experimentally accessed *in-situ* strains are marked by the red crosses (Methods). **e-j**, Band dispersions along  $\overline{MK}\overline{K}$  collected with *in-situ* nominal strains as indicated. Spectra in **h-j** are magnified around  $\overline{MK}$  near  $E_F$  and symmetrized with respect to  $k_y = 0$ . Superimposed are the extracted spectral peaks from both EDCs (circle markers) and MDCs (triangle markers), see details in Supplementary Fig. S9. **k**, Band dispersions from the extracted peaks as a function of strain. **l**, Polynomial fits for the two VHS-derived bands in **k** (Supplementary Fig. S10 and Methods). **m**, Strain dependence of the EDCs at  $\overline{M}$  point. The peak positions of  $VHS_{1,2}$  and flat band at  $\overline{M}$  (FBM) are indicated by the respective markers. **n**, Strain-dependent energy positions of  $VHS_{1,2}$  and FBM, as well as the second-order fitting coefficient ( $C_2$ ) of  $VHS_1$  band that is inversely proportional to its high-order character (Methods). Measurement temperature was set at 10 K and all spectra were divided by the Fermi-Dirac function, see Methods for more detailed experimental conditions. The spectral and strain colour bars represent ARPES intensities from high (H) to low (L) in arbitrary units and longitudinal uniaxial strain from compressive (blue) to tensile (red), respectively.

potential shift and suggest an orbital-selective bandwidth transfer. It is shown that the  $T_{CDW}$  can be strain-tuned [24]. We plot the mean-field CDW gap deduced by  $\Delta(\epsilon) = 3.5k_B T_{CDW}(\epsilon)$  in Supplementary Fig. S12a. Our results support a much faster CDW-gap suppression towards tensile direction, manifested by not only a triple reduction but also the absolute change of  $\sim 95$  meV (from  $\sim 150$  to 55 meV for  $\Delta_{\overline{M}\overline{K}}$ ) with only 1% strain (see also Fig. 5a). A giant strain response of the CDW order parameters is thus spectroscopically visualised.

The giant CDW response to a strain perturbation points to the unconventional nature of charge modulations in  $CsV_3Sb_5$ . Lattice distortions with a star-of-David pattern or its inverse counterpart are reported to coexist [27, 28] (see also Supplementary Fig. S6l-n and notes). CDW orders with different  $c$ -axis stackings are also observed [29, 30]. Such an intertwist of the CDW

supercells is likely sensitive to small lattice variations, in particular for a competing relationship [30]. These studies thus imply a possible strain-induced change of the charge-modulation patterns or stacking phases leading to the giant CDW response observed here. It is worth noting that, the strain-dependent observations were obtained at  $\sim 20$  K. The band structure exhibits nematic band foldings (Supplementary Fig. S5). Therefore, the reported CDW-driven electronic nematicity [15] or unidirectional charge order [16, 31] may also contribute to the observed gap openings and react with the uniaxial strain. The observations of nested Fermi-surface gaps and VHSs favour an electronic origin of the CDW (Fig. 2j,k). This further conforms the recent Ginzburg-Landau minimal model proposing a charge bond order (CBO) driven by the sublattice-assisted Fermi-surface instability [32]. Threefold CBO has a tendency of unfolding

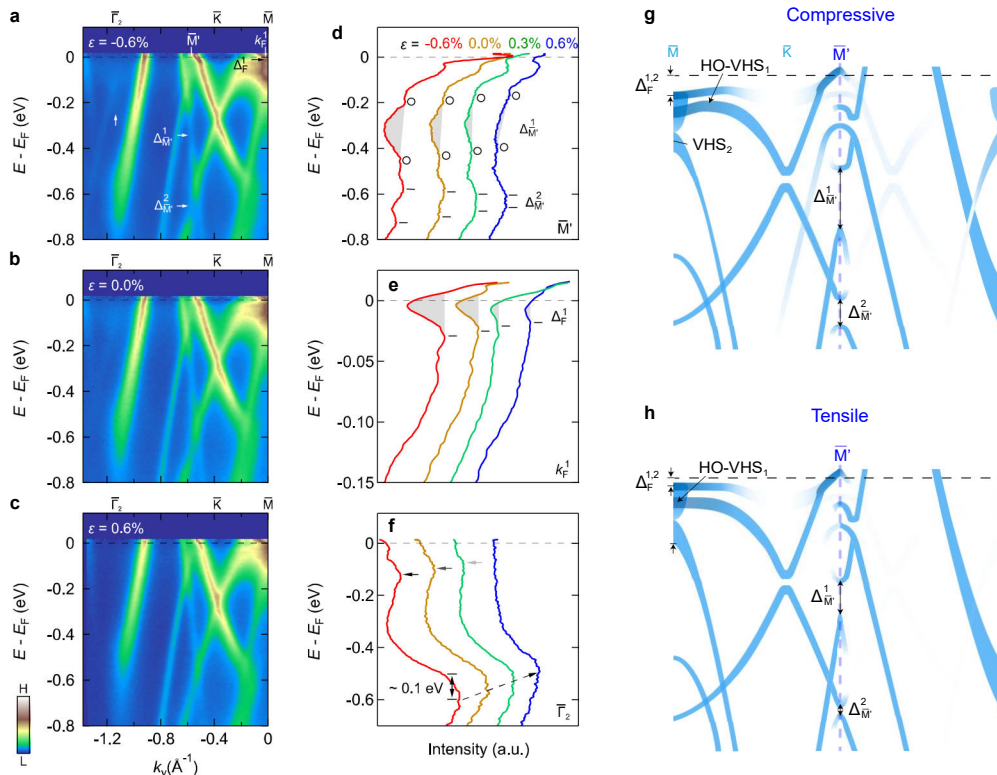


FIG. 4. **Strain tuning of the CDW.** **a-c**, Magnified  $\overline{MKT}$  dispersions with strain  $\epsilon$  as indicated. CDW-folded bands (vertical arrow) and CDW-related gaps as well as corresponding momentum positions are indicated in **a**. **d-f**, Strain dependences of EDCs at  $\overline{M}'$ ,  $k_F^1$ , and  $\overline{\Gamma}_2$ . The bars or circles in **d,e** indicate the positions of quasi-particle peaks or spectral shoulders. The shaded areas in **d,e** represent spectral-weight suppressions for  $\Delta_{\overline{M}'}^1$  and  $\Delta_{\overline{\Gamma}_2}^1$  (Methods). Horizontal short arrows in **f** mark the CDW folding bands vanishing with tensile strain, while long dashed arrow indicates an energy shift ( $\sim 0.1$  eV) of the band bottom. **g,h**, Schematics of the band structure in response to uniaxial strain applied along  $\overline{\Gamma M}$ . Vertical arrows indicate either energy gaps or energy shifts. Measurement temperature was set at 10 K and all spectra were divided by the Fermi-Dirac function, see Methods for more detailed experimental conditions. The colour bar represents ARPES intensities from high (H) to low (L) in arbitrary units.

into various orders. A chiral charge order is energetically preferred. The lattice perturbation can be a tuning knob for such phase transitions. Our results thus provide a natural interpretation for the conflicting reports of chiral CDW states [13, 33], which likely stem from the residual local strain. Additionally, our current studies also suggest the indispensable role of electron-phonon coupling (EPC) bridging the lattice perturbations to electronic responses. Significant EPC kinks were indeed found in  $AV_3Sb_5$  [23, 34] (Supplementary Fig. S6e,k and notes). We leave its detailed strain effects for a future work.

A minor lattice perturbation is generally not expected to generate giant changes for a system stabilizing at its minimum free-energy state. Here we highlight the important role of proximity to a high-order singularity [18]. The strain response of HO-VHS<sub>1</sub> is manifested by its rapid mass enhancement (band flattening in Fig. 3l) with a drop of the band curvature ( $C_2$  in Fig. 3n). Qualitatively, the band flatness or normalized effective mass can be represented as  $1-C_2$ . As such, we plot  $1-C_2$  as func-

tions of strain (Fig. 5a) and the CDW gap (Fig. 5b). A dramatic enhancement of the mass is accompanied simultaneously with an instant CDW suppression towards the tensile direction (Fig. 5a). The mass enhancement of HO-VHS<sub>1</sub> reveals a nearly ideal HO-VHS achieved by a fine strain tuning (see also Fig. 3l). The anticorrelation between the HO-VHS<sub>1</sub> and CDW order parameter (Fig. 5b) naturally explains the splitting of VHS<sub>1</sub> arising from CDW renormalizations [35] (Fig. 3l). These observations demonstrate a rare example of strain sensitive HO-VHS with strong electronic correlations coupling to an unconventional charge modulation. The CDW and SC orders are believed to compete in the  $CsV_3Sb_5$  system [10]. The anticorrelation between the CDW and HO-VHS<sub>1</sub>, therefore, implies a supportive connection of the latter to the underlying SC. Indeed, the SC  $T_c$  is reported to increase under tensile strain (Fig. 5b) [24]. Correspondingly, we uncover an enhanced DOS and electronic correlations at  $E_F$ , arising from the mass enhancement and energy lift of the HO-VHS<sub>1</sub> (Fig. 5b). These ob-

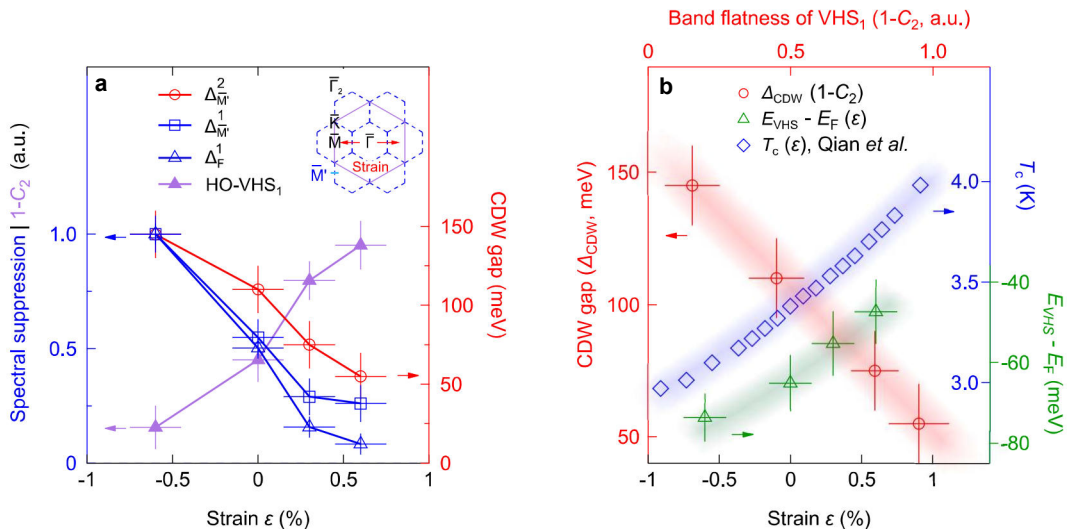


FIG. 5. **Giant strain response of CDW order parameter and its anticorrelation with HO-VHS.** **a**, Energy gaps and normalized spectral-weight suppressions as a function of uniaxial strain  $\epsilon$ . Plotted together is the HO character of VHS<sub>1</sub> represented by  $1-C_2$ , demonstrating its band flatness or qualitatively the normalized effective mass (purple markers). The inset shows a schematic CDW BZ and the direction of applied strain as indicated by the arrow. **b**, Strain-dependent CDW gap ( $\Delta_{\text{CDW}}$ ) versus the band flatness of VHS<sub>1</sub> ( $1-C_2$ ). The energy positions of HO-VHS<sub>1</sub> ( $E_{\text{VHS}} - E_F$ , Fig. 3n) and SC  $T_c$  (Qian *et al.* [24]) are plotted as a function of strain for comparisons.

servations suggest an intimate connection between the HO-VHS<sub>1</sub> and the SC order. Our results thus shed light on the important role of a HO-VHS in the SC pairing mechanism of CsV<sub>3</sub>Sb<sub>5</sub>.

As a reversible, flexible, disorder-free, and single-parameter tuning knob, uniaxial strain has demonstrated its highly desirable role in engineering quantum materials [1–5]. Given the numerous reports showing a strain sensitivity in AV<sub>3</sub>Sb<sub>5</sub> [14, 36, 37], our direct observations of giant electronic responses reveal a rich strain tunability on such a versatile platform inspiring further studies of quantum interplays under lattice perturbations.

## Methods

**Samples.** High-quality CsV<sub>3</sub>Sb<sub>5</sub> single crystals were grown by the modified self-flux method [6, 31]. To facilitate uniaxial strain application, the crystals were cut into a rectangular shape with in-plane dimension  $\sim 1 \times 0.8$  mm<sup>2</sup>.

**ARPES.** ARPES measurements were performed at the beamline I05 of Diamond Light Source in UK and beamline Bloch of MAX IV Laboratory in Sweden. Samples were mounted using silver epoxy and cleaved by standard top-post method *in-situ*. Beam spot sizes were set at  $\sim 50 \times 50$  and  $10 \times 5$   $\mu\text{m}^2$ , respectively. Photon energies were scanned from  $\sim 40$  eV to 100 eV to assign the high-symmetry  $k_z$  points (Supplementary Fig. S1). To access dominant spectral weights at  $k_z \sim 0$   $\pi/c$ , photon energy was set at 82 eV with overall energy resolution 12 – 16 meV. Both linear horizontal and vertical

light polarizations were utilised to obtain the entire band structure with high contrasts (Fig. 2). Electron analysers with vertical slits are MBS A-1 from MB Scientific AB and DA30L from ScientaOmicron, respectively, with angular resolutions 0.1 – 0.2°. Photoelectron emission angles were scanned by a step of 0.1° to precisely locate the momentum positions. Low (high) temperature measurements were conducted in vacuum conditions with pressures better than  $1.5 \times 10^{-10}$  ( $2 \times 10^{-10}$ ) mbar and  $8 \times 10^{-11}$  ( $1 \times 10^{-10}$ ) Torr, respectively.

**ARPES analysis.** Figure 1j,m and Fig. 2c,d are composed by two spectra collected along orthogonal paths. Owing to the surface sensitivity and quasi-2D structure, surface BZ is utilised (Fig. 1c). *Spectral symmetrization* is adopted in Fig. 1e,g and Fig. 2k to minimize matrix-element effect in Fermi surfaces, and in Fig. 4a-c to reduce noise. Fermi-surface symmetrizations were done by assuming only mirror symmetries with respect to  $\bar{M}\bar{K}$  and  $\bar{\Gamma}\bar{M}$  owing to the possible nematic states at low temperature. *Fermi-Dirac function division* (FDD) is utilised throughout this study, i.e., the spectra were divided by a Fermi-Dirac function that is convolved with a Gaussian representing the energy resolution [38], which effectively removes the Fermi cutoff and recovers the single-particle spectral function to the extent allowed by thermal population (Supplementary Fig. S3). On the other hand, energy gaps revealed after recovering spectral functions do not assume particle-hole symmetry which is typically broken in the CDW state. *Curvature or second-derivative analysis* [39] is adopted to enhance band visualisation in

Fig. 2d. These methods inevitably produce “peaks” or “flat bands” below  $E_F$  due to Fermi cutoffs (Supplementary Fig. S3e,g). To alleviate such artifacts near  $E_F$ , FDD spectra are utilised when performing the analysis. *CDW gap magnitudes* of  $\Delta_M^1$  and  $\Delta_F^1$  are defined as spectral-weight suppressions, represented by the grey shaded areas in Fig. 3j,k. ARPES spectral weights contain rich information of intertwined states in correlated systems [38, 40, 41], which is also in general proportional to DOS at a given condition. A spectral-weight suppression is therefore directly linked to DOS depletion representing a phase coherence or order parameter that can be utilised to quantify energy gaps especially in a partial gap scenario [40]. *Spectral peaks* of energy/momentum distribution curves (EDCs/MDCs) are extracted by analysing either first/second derivatives [42] or fittings to the multi-peak Lorentzian statistics, with error lbars estimated in accordance with the smoothness and widths of peaks (Supplementary Fig. S4,S9). *Fermi momenta*  $k_F$  are obtained from Lorentzian fittings to MDCs at  $E_F$  at high temperatures.  $k_F$  in Fig. 2e,g,i are determined in conjunction with the CB and VB  $E_F$  crossings in Fig. 2j. *Polynomial fits* of VHSs were done using  $\omega(k) = C_0 + C_2 \cdot k^2 + C_4 \cdot k^4 + \dots$  with  $C_n$  denoting the  $n$ -th order fitting coefficients (Supplementary Fig. S10). The band flatness near the vicinity of VHS is controlled by  $\omega(k)''|_{k=0} = 2C_2$ . A flatter VHS is therefore associated with smaller  $C_2$  and non-zero high-order terms, i.e., HO-VHS. The error bars of  $C_2$  in Fig. 5a are fitting standard deviations.

**Strain device.** Our new uniaxial strain device is based on a customized bendable sample platform that enables *in-situ* applications of more than  $\pm 3\%$  compressive or tensile strain. The design is composed of a T-shape platform, a step-like actuator, a driving screw with a circlip, and a customized omicron holder. All components are non-magnetic and typically made of BeCu with excellent elastic, thermal, and electric properties. As shown in Fig. 3a,b, by tightening the driving screw, the actuator is pushed down and therefore enforces a downward bending of the edge-connected platform providing tensile strain along the platform. Loosing the driving screw lifts the actuator driven by the underneath circlip which upward bends the platform realizing a compression. Such a driving mechanism enables a compact and flexible cell that fits spectroscopic manipulators.

**Strain evaluation.** The *in-situ* strain controls were realised by rotating the driving screws using equipped wobble stick. Strain evaluation follows the previous report, in which a precise connection between the real strain magnitude measured by the commercial gauges and the finite-element simulated strain size was well established [5]. Therefore, the strain magnitudes at the sample position as a function of driving-screw angle can be simulated as shown in Fig. 3d. The strain magnitudes *in-situ* con-

trolled in ARPES measurements were then evaluated by interpolating the strain–angle curve at the corresponding screw angles (red markers in Fig. 3d). The error bars for the strain magnitude in Fig. 3n and Fig. 5a include the uncertainties of screw angles and thermal contractions.

**DFT Calculations.** Density functional theory calculations have been performed using the Vienna ab-initio simulation package (VASP) [43], within the projector-augmented plane-wave (PAW) method [44]. When dealing with the  $\text{CsV}_3\text{Sb}_5$  unit cell, the Kohn-Sham wave functions are expanded into plane waves up to an energy cutoff of 600 eV, using the PBE-GGA functional to handle the exchange-correlation potential [45]. The Brillouin zone has been sampled with a  $12 \times 12 \times 8$   $\Gamma$ -centered  $k$ -mesh including spin-orbit coupling self-consistently, when present. The relaxation of the electronic degrees of freedom was considered converged when the energy difference among two steps was equal or smaller than  $1.0^{-6}$  eV. To compute the partial occupancies it was used a Gaussian smearing with a width of 0.02 eV. In order to determine, as a function of the applied uniaxial strain, the positions of the Dirac cones as well as their gap values at K, we performed non self-consistent calculations with a number of  $k$ -points ranging among 1024 and 2048 along the path  $\Gamma$ -K-M- $\Gamma$ , where the cones are moving. When considering the  $2 \times 2 \times 1$  ISD and SD supercells, the the Kohn-Sham wave functions are expanded into plane waves up to an energy cutoff of 400 eV. Band structures have been visualized using the VASPKIT postprocessing tool [46]. VESTA [47] has been used to visualize crystal structures.

## Acknowledgements

C.L., J.K., and J.C. acknowledge support from the Swiss National Science Foundation (Projects No. 200021.188564). C.L. and M.M.D. thank the support from Forschungskredit of the University of Zurich under grant numbers FK-22-119 and FK-22-085, respectively. O.K.F. is supported by the Swedish Research Council (VR) via a Grant 2022-06217 and the Foundation Blanceflor 2023 fellow scholarship. J.K. is supported by a Ph.D. fellowship from the German Academic Scholarship Foundation. A.C. and G.S. acknowledge the Gauss Centre for Supercomputing e.V. (<https://www.gauss-centre.eu>) for funding this project by providing computing time on the GCS Supercomputer SuperMUC-NG at Leibniz Supercomputing Centre (<https://www.lrz.de>). A.C. and G.S. are also grateful for funding support from the Deutsche Forschungsgemeinschaft (DFG, German Research Foundation) under Germany’s Excellence Strategy through the Würzburg-Dresden Cluster of Excellence on Complexity and Topology in Quantum Matter ct.qmat (EXC 2147, Project ID 390858490) as well as through the Collaborative Research Center SFB 1170 ToCoTronics (Project ID 258499086). Z.G. acknowledges support from

the Swiss National Science Foundation (SNSF) through SNSF Starting Grant (No. TMSGI2\_211750). We acknowledge MAX IV Laboratory for time on Beamline Bloch under Proposal 20221475. Research conducted at MAX IV, a Swedish national user facility, is supported by the Swedish Research council under contract 2018-07152, the Swedish Governmental Agency for Innovation Systems under contract 2018-04969, and Formas under contract 2019-02496. We acknowledge Diamond Light Source for time on Beamline I05 under Proposals SI30650 and SI33528.

### Author contributions

J.C. and C.L. conceived the project. C.L. carried out the ARPES experiments with supports from O.K.F., J.K., J.C., D.C., M.L., C.P., B.T., A.L., M.W., T.K., and C.C.. C.L. designed the uniaxial strain device with supports from J.C.. C.L. analysed the data and performed the strain evaluations. A.C. calculated the band structure with supports from M.M.D., G.S., and T.N.. H.L. and Z.G. provided the single crystals. C.L., A.C., and J.C. wrote the manuscript with inputs from all authors. All authors discussed the results and commented on the manuscript.

### Data availability

The data that support the findings of this study are available from the corresponding author upon request.

### Competing interests

The authors declare no competing interests.

- 
- [1] J.-H. Chu, J. G. Analytis, K. D. Greve, P. L. McMahon, Z. Islam, Y. Yamamoto, and I. R. Fisher, In-Plane Resistivity Anisotropy in an Underdoped Iron Arsenide Superconductor, *Science* **329**, 824 (2010).
- [2] D. Flötotto, Y. Bai, Y.-H. Chan, P. Chen, X. Wang, P. Rossi, C.-Z. Xu, C. Zhang, J. A. Hlevyack, J. D. Denlinger, H. Hong, M.-Y. Chou, E. J. Mittemeijer, J. N. Eckstein, and T.-C. Chiang, In Situ Strain Tuning of the Dirac Surface States in Bi<sub>2</sub>Se<sub>3</sub> Films, *Nano Lett.* **18**, 5628 (2018).
- [3] S. Riccò, M. Kim, A. Tamai, S. McKeown Walker, F. Y. Bruno, I. Cucchi, E. Cappelli, C. Besnard, T. K. Kim, P. Dudin, M. Hoesch, M. J. Gutmann, A. Georges, R. S. Perry, and F. Baumberger, In situ strain tuning of the metal-insulator-transition of Ca<sub>2</sub>RuO<sub>4</sub> in angle-resolved photoemission experiments, *Nat. Commun.* **9**, 4535 (2018).
- [4] V. Sunko, E. Abarca Morales, I. Marković, M. E. Barber, D. Milosavljević, F. Mazzola, D. A. Sokolov, N. Kikugawa, C. Cacho, P. Dudin, H. Rosner, C. W. Hicks, P. D. C. King, and A. P. Mackenzie, Direct observation of a uniaxial stress-driven Lifshitz transition in Sr<sub>2</sub>RuO<sub>4</sub>, *npj Quantum Mater.* **4**, 46 (2019).
- [5] C. Lin, M. Ochi, R. Noguchi, K. Kuroda, M. Sakoda, A. Nomura, M. Tsubota, P. Zhang, C. Bareille, K. Kurokawa, Y. Arai, K. Kawaguchi, H. Tanaka, K. Yaji, A. Harasawa, M. Hashimoto, D. Lu, S. Shin, R. Arita, S. Tanda, and T. Kondo, Visualization of the strain-induced topological phase transition in a quasi-one-dimensional superconductor TaSe<sub>3</sub>, *Nat. Mater.* **20**, 1093 (2021).
- [6] B. R. Ortiz, L. C. Gomes, J. R. Morey, M. Winiarski, M. Bordelon, J. S. Mangum, I. W. H. Oswald, J. A. Rodriguez-Rivera, J. R. Neilson, S. D. Wilson, E. Ertekin, T. M. McQueen, and E. S. Toberer, New kagome prototype materials: Discovery of KV<sub>3</sub>Sb<sub>5</sub>, RbV<sub>3</sub>Sb<sub>5</sub>, and CsV<sub>3</sub>Sb<sub>5</sub>, *Phys. Rev. Materials* **3**, 094407 (2019).
- [7] B. R. Ortiz, S. M. L. Teicher, Y. Hu, J. L. Zuo, P. M. Sarte, E. C. Schueller, A. M. M. Abeykoon, M. J. Krogstad, S. Rosenkranz, R. Osborn, R. Seshadri, L. Balents, J. He, and S. D. Wilson, CsV<sub>3</sub>Sb<sub>5</sub>: A Z<sub>2</sub> Topological Kagome Metal with a Superconducting Ground State, *Phys. Rev. Lett.* **125**, 247002 (2020).
- [8] Z. Liang, X. Hou, F. Zhang, W. Ma, P. Wu, Z. Zhang, F. Yu, J.-J. Ying, K. Jiang, L. Shan, Z. Wang, and X.-H. Chen, Three-Dimensional Charge Density Wave and Surface-Dependent Vortex-Core States in a Kagome Superconductor CsV<sub>3</sub>Sb<sub>5</sub>, *Phys. Rev. X* **11**, 031026 (2021).
- [9] H. Li, T. T. Zhang, T. Yilmaz, Y. Y. Pai, C. E. Marvinney, A. Said, Q. W. Yin, C. S. Gong, Z. J. Tu, E. Vescovo, C. S. Nelson, R. G. Moore, S. Murakami, H. C. Lei, H. N. Lee, B. J. Lawrie, and H. Miao, Observation of Unconventional Charge Density Wave without Acoustic Phonon Anomaly in Kagome Superconductors AV<sub>3</sub>Sb<sub>5</sub> (A = Rb, Cs), *Phys. Rev. X* **11**, 031050 (2021).
- [10] F. H. Yu, D. H. Ma, W. Z. Zhuo, S. Q. Liu, X. K. Wen, B. Lei, J. J. Ying, and X. H. Chen, Unusual competition of superconductivity and charge-density-wave state in a compressed topological kagome metal, *Nat. Commun.* **12**, 3645 (2021).
- [11] Y. Zhong, J. Liu, X. Wu, Z. Guguchia, J.-X. Yin, A. Mine, Y. Li, S. Najafzadeh, D. Das, C. Mielke, R. Khasanov, H. Luetkens, T. Suzuki, K. Liu, X. Han, T. Kondo, J. Hu, S. Shin, Z. Wang, X. Shi, Y. Yao, and K. Okazaki, Nodeless electron pairing in CsV<sub>3</sub>Sb<sub>5</sub>-derived kagome superconductors, *Nature* **617**, 488 (2023).
- [12] Z. Guguchia, C. Mielke, D. Das, R. Gupta, J.-X. Yin, H. Liu, Q. Yin, M. H. Christensen, Z. Tu, C. Gong, N. Shumiya, M. S. Hossain, T. Gamsakhurdashvili, M. Elender, P. Dai, A. Amato, Y. Shi, H. C. Lei, R. M. Fernandes, M. Z. Hasan, H. Luetkens, and R. Khasanov, Tunable unconventional kagome superconductivity in charge ordered RbV<sub>3</sub>Sb<sub>5</sub> and KV<sub>3</sub>Sb<sub>5</sub>, *Nat. Commun.* **14**, 153 (2023).
- [13] Y.-X. Jiang, J.-X. Yin, M. M. Denner, N. Shumiya, B. R. Ortiz, G. Xu, Z. Guguchia, J. He, M. S. Hossain, X. Liu, J. Ruff, L. Kautzsch, S. S. Zhang, G. Chang, I. Belopolski, Q. Zhang, T. A. Cochran, D. Multer, M. Litskevich, Z.-J. Cheng, X. P. Yang, Z. Wang, R. Thomale, T. Neupert, S. D. Wilson, and M. Z. Hasan, Unconventional chiral charge order in kagome superconductor KV<sub>3</sub>Sb<sub>5</sub>, *Nat. Mater.* **20**, 1353 (2021).
- [14] C. Guo, C. Putzke, S. Konyzheva, X. Huang, M. Gutierrez-Amigo, I. Errea, D. Chen, M. G. Vergniory, C. Felser, M. H. Fischer, T. Neupert, and P. J. W. Moll, Switchable chiral transport in charge-ordered kagome metal CsV<sub>3</sub>Sb<sub>5</sub>, *Nature* **611**, 461 (2022).

- [15] L. Nie, K. Sun, W. Ma, D. Song, L. Zheng, Z. Liang, P. Wu, F. Yu, J. Li, M. Shan, D. Zhao, S. Li, B. Kang, Z. Wu, Y. Zhou, K. Liu, Z. Xiang, J. Ying, Z. Wang, T. Wu, and X. Chen, Charge-density-wave-driven electronic nematicity in a kagome superconductor, *Nature* **604**, 59 (2022).
- [16] H. Zhao, H. Li, B. R. Ortiz, S. M. L. Teicher, T. Park, M. Ye, Z. Wang, L. Balents, S. D. Wilson, and I. Zeljkovic, Cascade of correlated electron states in the kagome superconductor CsV<sub>3</sub>Sb<sub>5</sub>, *Nature* **599**, 216 (2021).
- [17] C. Mielke III, D. Das, J.-X. Yin, H. Liu, R. Gupta, Y.-X. Jiang, M. Medarde, X. Wu, H. C. Lei, J. Chang, P. Dai, Q. Si, H. Miao, R. Thomale, T. Neupert, Y. Shi, R. Khasanov, M. Z. Hasan, H. Luetkens, and Z. Guguchia, Time-reversal symmetry-breaking charge order in a kagome superconductor, *Nature* **602**, 245 (2022).
- [18] N. F. Q. Yuan, H. Isobe, and L. Fu, Magic of high-order van Hove singularity, *Nat. Commun.* **10**, 5769 (2019).
- [19] M. Kang, S. Fang, J.-K. Kim, B. R. Ortiz, S. H. Ryu, J. Kim, J. Yoo, G. Sangiovanni, D. Di Sante, B.-G. Park, C. Jozwiak, A. Bostwick, E. Rotenberg, E. Kaxiras, S. D. Wilson, J.-H. Park, and R. Comin, Twofold van Hove singularity and origin of charge order in topological kagome superconductor CsV<sub>3</sub>Sb<sub>5</sub>, *Nat. Phys.* **18**, 301 (2022).
- [20] Y. Hu, X. Wu, B. R. Ortiz, S. Ju, X. Han, J. Ma, N. C. Plumb, M. Radovic, R. Thomale, S. D. Wilson, A. P. Schnyder, and M. Shi, Rich nature of Van Hove singularities in Kagome superconductor CsV<sub>3</sub>Sb<sub>5</sub>, *Nat. Commun.* **13**, 2220 (2022).
- [21] B. R. Ortiz, S. M. L. Teicher, L. Kautzsch, P. M. Sarte, N. Ratcliff, J. Harter, J. P. C. Ruff, R. Seshadri, and S. D. Wilson, Fermi Surface Mapping and the Nature of Charge-Density-Wave Order in the Kagome Superconductor CsV<sub>3</sub>Sb<sub>5</sub>, *Phys. Rev. X* **11**, 041030 (2021).
- [22] Z. Jiang, H. Ma, W. Xia, Z. Liu, Q. Xiao, Z. Liu, Y. Yang, J. Ding, Z. Huang, J. Liu, Y. Qiao, J. Liu, Y. Peng, S. Cho, Y. Guo, J. Liu, and D. Shen, Observation of Electronic Nematicity Driven by the Three-Dimensional Charge Density Wave in Kagome Lattice KV<sub>3</sub>Sb<sub>5</sub>, *Nano Lett.* **23**, 5625 (2023).
- [23] H. Luo, Q. Gao, H. Liu, Y. Gu, D. Wu, C. Yi, J. Jia, S. Wu, X. Luo, Y. Xu, L. Zhao, Q. Wang, H. Mao, G. Liu, Z. Zhu, Y. Shi, K. Jiang, J. Hu, Z. Xu, and X. J. Zhou, Electronic nature of charge density wave and electron-phonon coupling in kagome superconductor KV<sub>3</sub>Sb<sub>5</sub>, *Nat. Commun.* **13**, 273 (2022).
- [24] T. Qian, M. H. Christensen, C. Hu, A. Saha, B. M. Andersen, R. M. Fernandes, T. Birol, and N. Ni, Revealing the competition between charge density wave and superconductivity in CsV<sub>3</sub>Sb<sub>5</sub> through uniaxial strain, *Phys. Rev. B* **104**, 144506 (2021).
- [25] A. Consiglio, T. Schwemmer, X. Wu, W. Hanke, T. Neupert, R. Thomale, G. Sangiovanni, and D. Di Sante, Van Hove tuning of AV<sub>3</sub>Sb<sub>5</sub> kagome metals under pressure and strain, *Phys. Rev. B* **105**, 165146 (2022).
- [26] H. LaBollita and A. S. Botana, Tuning the Van Hove singularities in AV<sub>3</sub>Sb<sub>5</sub> ( $A = K, Rb, Cs$ ) via pressure and doping, *Phys. Rev. B* **104**, 205129 (2021).
- [27] M. Kang, S. Fang, J. Yoo, B. R. Ortiz, Y. M. Oey, J. Choi, S. H. Ryu, J. Kim, C. Jozwiak, A. Bostwick, E. Rotenberg, E. Kaxiras, J. G. Checkelsky, S. D. Wilson, J.-H. Park, and R. Comin, Charge order landscape and competition with superconductivity in kagome metals, *Nat. Mater.* **22**, 186 (2023).
- [28] Y. Hu, X. Wu, B. R. Ortiz, X. Han, N. C. Plumb, S. D. Wilson, A. P. Schnyder, and M. Shi, Coexistence of trihexagonal and star-of-David pattern in the charge density wave of the kagome superconductor AV<sub>3</sub>Sb<sub>5</sub>, *Phys. Rev. B* **106**, L241106 (2022).
- [29] H. Li, G. Fabbris, A. H. Said, J. P. Sun, Y.-X. Jiang, J.-X. Yin, Y.-Y. Pai, S. Yoon, A. R. Lupini, C. S. Nelson, Q. W. Yin, C. S. Gong, Z. J. Tu, H. C. Lei, J.-G. Cheng, M. Z. Hasan, Z. Wang, B. Yan, R. Thomale, H. N. Lee, and H. Miao, Discovery of conjoined charge density waves in the kagome superconductor CsV<sub>3</sub>Sb<sub>5</sub>, *Nat. Commun.* **13**, 6348 (2022).
- [30] Q. Xiao, Y. Lin, Q. Li, X. Zheng, S. Francoual, C. Plueckthun, W. Xia, Q. Qiu, S. Zhang, Y. Guo, J. Feng, and Y. Peng, Coexistence of multiple stacking charge density waves in kagome superconductor CsV<sub>3</sub>Sb<sub>5</sub>, *Phys. Rev. Res.* **5**, L012032 (2023).
- [31] H. Chen, H. Yang, B. Hu, Z. Zhao, J. Yuan, Y. Xing, G. Qian, Z. Huang, G. Li, Y. Ye, S. Ma, S. Ni, H. Zhang, Q. Yin, C. Gong, Z. Tu, H. Lei, H. Tan, S. Zhou, C. Shen, X. Dong, B. Yan, Z. Wang, and H.-J. Gao, Roton pair density wave in a strong-coupling kagome superconductor, *Nature* **599**, 222 (2021).
- [32] M. M. Denner, R. Thomale, and T. Neupert, Analysis of Charge Order in the Kagome Metal AV<sub>3</sub>Sb<sub>5</sub> ( $A = K, Rb, Cs$ ), *Phys. Rev. Lett.* **127**, 217601 (2021).
- [33] H. Li, H. Zhao, B. R. Ortiz, T. Park, M. Ye, L. Balents, Z. Wang, S. D. Wilson, and I. Zeljkovic, Rotation symmetry breaking in the normal state of a kagome superconductor KV<sub>3</sub>Sb<sub>5</sub>, *Nat. Phys.* **18**, 265 (2022).
- [34] Y. Zhong, S. Li, H. Liu, Y. Dong, K. Aido, Y. Arai, H. Li, W. Zhang, Y. Shi, Z. Wang, S. Shin, H. N. Lee, H. Miao, T. Kondo, and K. Okazaki, Testing electron-phonon coupling for the superconductivity in kagome metal CsV<sub>3</sub>Sb<sub>5</sub>, *Nat. Commun.* **14**, 1945 (2023).
- [35] S. Cho, H. Ma, W. Xia, Y. Yang, Z. Liu, Z. Huang, Z. Jiang, X. Lu, J. Liu, Z. Liu, J. Li, J. Wang, Y. Liu, J. Jia, Y. Guo, J. Liu, and D. Shen, Emergence of New van Hove Singularities in the Charge Density Wave State of a Topological Kagome Metal RbV<sub>3</sub>Sb<sub>5</sub>, *Phys. Rev. Lett.* **127**, 236401 (2021).
- [36] C. Guo, G. Wagner, C. Putzke, D. Chen, K. Wang, L. Zhang, M. Gutierrez-Amigo, I. Errea, M. G. Vergniory, C. Felser, M. H. Fischer, T. Neupert, and P. J. W. Moll, Correlated order at the tipping point in the kagome metal CsV<sub>3</sub>Sb<sub>5</sub>, *Nat. Phys.* , 1 (2024).
- [37] L. Yin, D. Zhang, C. Chen, G. Ye, F. Yu, B. R. Ortiz, S. Luo, W. Duan, H. Su, J. Ying, S. D. Wilson, X. Chen, H. Yuan, Y. Song, and X. Lu, Strain-sensitive superconductivity in the kagome metals KV<sub>3</sub>Sb<sub>5</sub> and CsV<sub>3</sub>Sb<sub>5</sub> probed by point-contact spectroscopy, *Phys. Rev. B* **104**, 174507 (2021).
- [38] M. Hashimoto, E. A. Nowadnick, R.-H. He, I. M. Vishik, B. Moritz, Y. He, K. Tanaka, R. G. Moore, D. Lu, Y. Yoshida, M. Ishikado, T. Sasagawa, K. Fujita, S. Ishida, S. Uchida, H. Eisaki, Z. Hussain, T. P. Devereaux, and Z.-X. Shen, Direct spectroscopic evidence for phase competition between the pseudogap and superconductivity in Bi<sub>2</sub>Sr<sub>2</sub>CaCu<sub>2</sub>O<sub>8+ $\delta$</sub> , *Nat. Mater.* **14**, 37 (2015).
- [39] P. Zhang, P. Richard, T. Qian, Y.-M. Xu, X. Dai, and H. Ding, A precise method for visualizing dispersive

- features in image plots, *Rev. Sci. Instrum.* **82**, 043712 (2011).
- [40] T. Kondo, R. Khasanov, T. Takeuchi, J. Schmalian, and A. Kaminski, Competition between the pseudogap and superconductivity in the high-Tc copper oxides, *Nature* **457**, 296 (2009).
- [41] T. Kondo, A. D. Palczewski, Y. Hamaya, T. Takeuchi, J. S. Wen, Z. J. Xu, G. Gu, and A. Kaminski, Formation of Gapless Fermi Arcs and Fingerprints of Order in the Pseudogap State of Cuprate Superconductors, *Phys. Rev. Lett.* **111**, 157003 (2013).
- [42] M. Hashimoto, R.-H. He, K. Tanaka, J.-P. Testaud, W. Meevasana, R. G. Moore, D. Lu, H. Yao, Y. Yoshida, H. Eisaki, T. P. Devereaux, Z. Hussain, and Z.-X. Shen, Particle-hole symmetry breaking in the pseudogap state of Bi2201, *Nat. Phys.* **6**, 414 (2010).
- [43] G. Kresse and J. Furthmüller, Efficient iterative schemes for ab initio total-energy calculations using a plane-wave basis set, *Phys. Rev. B* **54**, 11169 (1996).
- [44] P. E. Blöchl, Projector augmented-wave method, *Phys. Rev. B* **50**, 17953 (1994).
- [45] J. P. Perdew, K. Burke, and M. Ernzerhof, Generalized Gradient Approximation Made Simple, *Phys. Rev. Lett.* **77**, 3865 (1996).
- [46] V. Wang, N. Xu, J.-C. Liu, G. Tang, and W.-T. Geng, VASPKIT: A user-friendly interface facilitating high-throughput computing and analysis using VASP code, *Computer Physics Communications* **267**, 108033 (2021).
- [47] K. Momma and F. Izumi, VESTA: A three-dimensional visualization system for electronic and structural analysis, *J Appl Cryst* **41**, 653 (2008).